

# INVESTIGATION OF THE $\gamma/\gamma'$ MORPHOLOGY AND INTERNAL STRESSES IN A MONOCRYSTALLINE TURBINE BLADE AFTER SERVICE: DETERMINATION OF THE LOCAL THERMAL AND MECHANICAL LOADS

Horst Biermann, Berthold von Grossmann, Thomas Schneider, Hua Feng and Haël Mughrabi

Institut für Werkstoffwissenschaften, Lehrstuhl I, Universität Erlangen-Nürnberg,

Martensstr. 5, D-91058 Erlangen, Fed. Rep. Germany

## Abstract

In the present work, a procedure is presented which allows the determination of the locally acting loads during service of a turbine blade by detailed investigations of its microstructure. The microstructural characterization of a monocrystalline turbine blade of the nickel-base superalloy CMSX-6 subjected to service-like conditions was performed with different, complementary techniques. The morphology of the turbine blade was investigated with conventional scanning and transmission electron microscopy. Lattice parameter changes and the lattice distortions were measured by a special high-resolution X-ray diffraction method and by convergent beam electron diffraction.

The investigation of the microstructure of the turbine blade showed in some regions of the blade the build-up of a marked raft structure, especially near the leading and trailing edges. The investigations of local lattice parameter changes yielded lattice distortions in both phases  $\gamma$  and  $\gamma'$  which are attributed to residual deformation-induced and thermally induced long-range internal stresses. Using finite element calculations, lattice distortions were calculated for characteristic positions within the blade on the basis of the actual microstructure. The calculated lattice parameter distributions were compared with X-ray line profiles measured locally at the same points. The investigations showed that the microstructure and the lattice parameter distributions are determined mostly by the centrifugal stresses and the high material temperatures. A result of the convergent beam electron diffraction investigations obtained on the turbine blade was that the evaluation of the higher order Laue zone lines yielded local lattice distortions of the two phases.

## Introduction and Objectives

Two-phase nickel-base superalloy turbine blades are subjected locally to complex triaxial stresses during service. These stresses result from the superposition of centrifugal stresses which are acting in the [001] direction, the internal stresses on a microstructural scale and thermomechanical fatigue. Due to the difference of the lattice parameters  $a^\gamma$  and  $a^{\gamma'}$  and/or the different thermal expansion coefficients of the phases  $\gamma$  and  $\gamma'$ , coherency stresses and thermal stresses exist already in the initially undeformed state, e.g. [1-3]. During service of nickel-base superalloy turbine blades, changes of the  $\gamma/\gamma'$  morphology occur. In those regions of the turbine blades exposed to high temperatures, especially at the leading and trailing edges, directional coarsening of the  $\gamma'$  precipitates occurs, and a raft-like  $\gamma/\gamma'$  plate structure can develop [4-7].

Thermal stresses, coherency stresses and deformation-induced long-range internal stresses were evaluated from room temperature and high-temperature X-ray and neutron line profile measurements in undeformed and creep-deformed samples [2, 3, 8-13]. Investigations of the line profiles measured on samples creep deformed to different strains showed that the change of the lattice parameters due to internal stresses is completed after the creep rate has reached its minimum, i.e. after strains which are comparable to those experienced by the blade [5]. The investigations [5-7] showed that internal stresses can be measured by X-ray diffraction in turbine blades exposed to service. These internal stresses were attributed mostly to creep deformation experienced by the blade due to the centrifugal stresses during service. Further work proved the existence of internal stresses in nickel-base superalloys on a microscopical scale by the analysis of interfacial dislocation networks [14] and by convergent beam electron diffraction (CBED) [15, 16]. Finally, long-range internal stresses in the phases  $\gamma$  and  $\gamma'$  in creep-deformed samples were calculated by the finite element method (FEM) [17, 18].

This background provides the motivation for the present work on turbine blades that had been exposed to service-like conditions. The approach consists of a detailed quantitative microstructural characterization whose results are compared with available data on well-characterized laboratory specimens (with defined mechanical history) and are then used as input data for a FEM evaluation of the local triaxial stress and strain states in critical parts of the blade. The ultimate aim is to quantify the locally acting load states (i.e. the local temperatures and stresses) and to relate them to the locally experienced thermal and mechanical loading history.

In this paper, results of 3-dimensional FEM calculations of local lattice parameters and lattice mismatch values (the lattice mismatch  $\delta$  is defined as the relative difference of the lattice parameters of the phases  $\gamma'$  and  $\gamma$ ,  $\delta = 2(a^{\gamma'} - a^\gamma)/(a^{\gamma'} + a^\gamma)$ ) in the principal  $\langle 100 \rangle$  directions in a CMSX-6 turbine blade which has been exposed to service are reported. For this purpose, the  $\gamma/\gamma'$  microstructure of the turbine blade is evaluated quantitatively by scanning electron microscopy. The results of the modelling are compared with X-ray line profiles, which were measured at different positions within the turbine blade. The comparison of the X-ray line profiles and the calculated lattice parameter distributions of the turbine blades with data obtained on samples creep-deformed in tension provides evidence on the type of deformation experienced by the investigated parts of the turbine blades. Thus, the local loads under service of the turbine blade can be estimated from an adaptation of the input of the FEM model with the aim to obtain a good correlation between the calcu-

lated lattice parameters and the measured X-ray profiles. The existence of local strains in the two phases is investigated with high lateral resolution by convergent beam electron diffraction experiments by the analysis of the higher order Laue zone lines (HOLZ lines).

### Internal stresses

Measurements of local strains indicate a complex interaction of different contributions. These are i) coherency stresses which are present even in the initial state, ii) thermal stresses arising during cooling and iii) residual deformation-induced internal stresses. In the following, these different contributions are discussed in more detail.

### Coherency and thermal stresses

In the undeformed, standard heat-treated state, the ordered  $\gamma'$  phase is coherently precipitated in the  $\gamma$  matrix. Since most nickel-base superalloys have a misfit at room temperature in the order of  $10^{-3}$ , there are marked internal coherency stresses. At the high deformation temperatures, the misfit decreases due to the smaller thermal expansion coefficient of the  $\gamma'$  phase and is negative in the alloys used in practice. In the case of a negative lattice misfit, the  $\gamma$  phase is under the action of compressive stresses and the  $\gamma'$  phase under the action of tensile stresses. After long-term annealing at high temperatures, the coherency stresses are reduced by interfacial dislocations. The spacings of these dislocations which are arranged in regular dislocation networks can be evaluated to obtain the lattice misfit at the annealing temperature based on a relation stated by Brooks [19]. With the Brooks formula the lattice misfit can be determined from the Burgers vector  $b$  and the dislocation spacings  $d$ :  $\delta = |b|/d$ .

Anisotropic thermal stresses arise after raft formation due to the different thermal expansion coefficients of the two phases  $\gamma$  and  $\gamma'$  [2, 3]. The thermal stresses after deformation and cooling to room temperature are of compressive (tensile) nature in the  $\gamma'$  phase ( $\gamma$  phase), since the  $\gamma'$  phase has the smaller thermal expansion coefficient. These thermal stresses act in the plane of the  $\gamma$  and  $\gamma'$  plates, i.e. in the directions [100] and [010]. Therefore, the thermal stresses cause tetragonal lattice distortions of the two phases at room temperature in the raft structure.

### Deformation-induced internal stresses

Due to the different strengths of the two phases  $\gamma$  and  $\gamma'$  (see e.g. [20]), deformation-induced long-range internal stresses arise during deformation which prevail after unloading (cf. [8-12]). They are built up by interface dislocations [8, 16, 21] which form dislocation networks during deformation from strains of about 1 % onwards.

After tensile creep deformation in the [001] direction, the interface dislocations at (001) interfaces have the same nature as dislocations which relieve the coherency stresses in the case of a negative lattice misfit, see Figure 1(a). The faint lines in the figure represent the traces of the glide planes of the active slip systems. The lines are dashed in the ordered  $\gamma'$  phase, since dislocation activity concentrates mostly in the softer  $\gamma$  phase. The actual dislocation networks at the (001) interfaces reduce the coherency stresses. These dislocation networks also build up additional deformation-induced stresses which are of opposite sign compared to the coherency stresses (the coherency stresses are of compressive nature in the directions [100] and [010], the deformation-induced internal stresses, e.g., of tensile nature in  $\gamma$ , cf. Figure 1(b)). The interface dislocations at (100)/(010) interfaces do not reduce the coherency stresses, but they

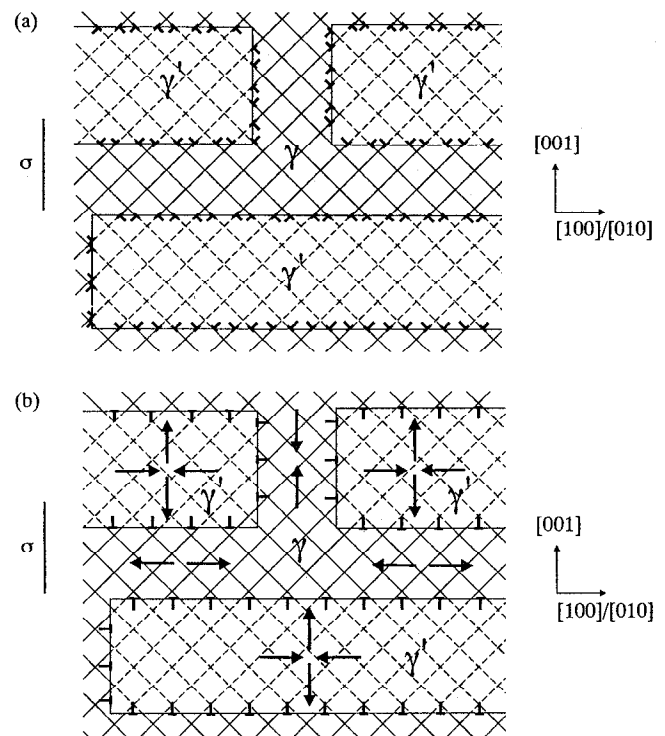


Figure 1: Idealized  $\gamma/\gamma'$  microstructure with resultant interface dislocations.  $\sigma$  shows the axis of the centrifugal stress (i.e. the [001] direction). (a) Accumulation of glide dislocations at the  $\gamma/\gamma'$  interfaces. (b) Resultant interface dislocations which put the two phases under internal stresses as indicated schematically by arrows. After [8].

cause additional deformation-induced internal stresses. Figure 1(b) shows the effect of the interfacial dislocation networks on the lattice parameters of the two phases. The addition of the Burgers vectors of adjacent pairs of the edge dislocations from symmetrical slip systems (Figure 1(a)) gives the resultant dislocations of Figure 1(b) with Burgers vectors parallel to the interfaces. These resultant edge dislocations are of different nature: i) Dislocations at the interfaces perpendicular to the stress axis have their extra half-plane in the  $\gamma'$  phase, ii) dislocations at the interfaces parallel to the stress axis in the  $\gamma$  phase. The  $\gamma'$  phase ( $\gamma$  phase) is under tensile strain (compressive strain) in the direction [001] and under compressive strain (tensile strain) in the directions [100] and [010], as indicated schematically by arrows. It has to be noted that in Figure 1 a microstructure is shown, where  $\gamma'$  plates are embedded in a  $\gamma$  matrix phase. This is in contrast to the drawing for creep-deformed samples in Reference [8], where the situation is reversed and  $\gamma$  plates are embedded in the  $\gamma'$  phase.

## Experimental

### Turbine blade

A monocrystalline turbine blade of the "light" nickel-base superalloy CMSX-6 with an orientation near [001] from a developmental turbine was investigated. The blade had been exposed to service for several hundred hours in two test turbines. The turbines have been operated in so-called accelerated mission tests. Local stresses acting during service were calculated analytically. The calculated local centrifugal stresses in the [001] direction experienced by the blade

during service at the investigated (001) section II (see Figure 2) were between 40 MPa and 230 MPa. In Figure 3, the local stress data are given for the investigated sites of section II. The turbine blade was sectioned and polished carefully mechanically parallel to the (001) lattice planes (the investigated cross sections are indicated in Figure 2) and to the (100) and (010) lattice planes.

### Electron microscopy

**Scanning electron microscopy.** The sections mentioned in the last paragraph were etched with a solution of H<sub>2</sub>O, HCl, MoO<sub>3</sub> and HNO<sub>3</sub> which etches preferentially the  $\gamma'$  phase. Subsequently, the sections were sputtered with gold. The investigations were performed with a scanning electron microscope at an accelerating voltage of 20 kV using back scattered electrons and evaluated for the particle size distributions of the phases  $\gamma'$  and  $\gamma$  using a digitizing table.

**Transmission electron microscopy and convergent beam electron diffraction (CBED).** From the sections investigated by SEM, thin slices with the orientations (001) and (100) were prepared for the TEM investigations. They were polished mechanically to a thickness of about 100  $\mu\text{m}$  and thinned electrolytically by a mixture of

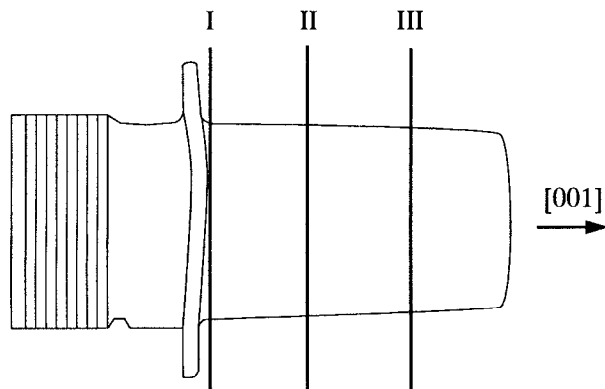


Figure 2: Schematic representation of the turbine blade. The marked sections I, II and III have been investigated in detail.

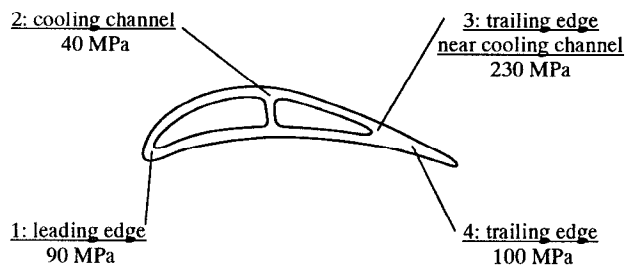


Figure 3: Local load data at the sites 1 (leading edge) to 4 (trailing edge) calculated analytically for section II, see Figure 2 (schematic drawing of the cross section).

methanol, butanol and perchloric acid at a temperature of  $-40\text{ }^{\circ}\text{C}$ . Since the CBED technique is very sensitive on thickness variations, some of the TEM samples were subsequently thinned by an ion thinning device. The TEM investigations were performed with an electron microscope of the type Philips CM 200. The TEM micrographs were taken at an accelerating voltage of 200 kV.

The CBED investigations were performed in the microscope at an accelerating voltage of 120 kV using a double tilt cooling stage at a temperature of  $-170\text{ }^{\circ}\text{C}$ . The use of the cooling stage improves the contrast of the HOLZ line and reduces contamination of the samples. Cooling has no noteworthy effect on the strains in the TEM foil, since the two phases  $\gamma$  and  $\gamma'$  have equal thermal expansion coefficients below about 500 to 600  $^{\circ}\text{C}$ . The electron beam was focussed to a diameter of about 20 nm. In the investigations presented in this paper, the [100] zone axis was used for different reasons (see also the work of Keller et al. [15]). i) The  $\langle 100 \rangle$  directions are distinguished directions of the raft structure. ii) The principal strains and stresses act in these directions (the centrifugal stress acts in [001]). iii) Relaxation of the internal stresses which could lead to angular distortions of the angles  $\alpha$ ,  $\beta$  and  $\gamma$  of the unit cells are minimal for foil preparation in the  $\{100\}$  planes. Due to these advantages, the [100] zone axis was investigated. In a first approximation, the observed patterns were simulated using a kinematical computer simulation [22]. Preliminary dynamical simulations, however, showed pronounced effects of dynamical scattering on the line positions in the  $\langle 100 \rangle$  zone axes. Therefore, in the present work, the measured patterns are discussed qualitatively, and no quantitative results are drawn.

### X-ray diffraction

X-ray line profile measurements of the  $\{200\}$  type Bragg reflections were performed on a special high-resolution double-crystal diffractometer with high angular resolution and negligible instrumental line broadening, using the  $\text{CuK}_{\alpha 1}$  radiation. The cross section of the X-ray beam was limited in order to obtain high lateral resolution. Therefore, the investigated surface of the blade was about 0,5 mm  $\times$  0,5 mm. The measured X-ray line profiles were separated into the subprofiles of the phases  $\gamma$  and  $\gamma'$  by a simple mirror technique. The setup of the diffractometer and the evaluation of the line profiles are described in detail in Reference [8].

### Finite Element Calculations

The FEM calculations were performed on workstations using the FEM program MARC K6.1/MENTAT 2.0. One eighth of a  $\gamma'$  particle with the surrounding matrix was divided in a 3-dimensional model by  $10 \times 10 \times 10$  elements consisting of 8 integration points. In the present case of the turbine blade, the  $\gamma$  phase still surrounds the  $\gamma'$  particles, in contrast to the creep-deformed samples investigated in Reference [18]. A further difference to the calculations of Ref. [18] is that in the present case plastic back flow of the  $\gamma$  phase during cooling is not considered, since the blades cool down to lower temperatures under centrifugal stresses.

Relevant input parameters of the FEM model are the dimensions of the finite element mesh, the thermal expansion coefficients of the phases  $\gamma$  and  $\gamma'$ , the anisotropic elastic constants of the two phases and the lattice misfit obtained from the spacings of dislocations in the interfacial dislocation networks on the  $\gamma/\gamma'$  interfaces. These parameters are explained in the next paragraph in detail.

**Input parameters.** The dimensions of the FEM models for the different modelled points were obtained from a quantitative evaluation of the microstructure at these positions. Available thermal expansion coefficients of the phases  $\gamma$  and  $\gamma'$  of the alloy SRR 99 were obtained from X-ray measurements of bulk SRR 99 samples. The use of bulk superalloy specimens has the advantage that the dissolution of the  $\gamma'$  phase at high temperatures is taken into consideration. This is not possible in the case of separate  $\gamma$  and  $\gamma'$  samples. The difference of the expansion coefficients of the phases  $\gamma$  and  $\gamma'$  between the two alloys SRR 99 and CMSX-6 is assumed to be small, because the expansion coefficients of the bulk alloys differ only slightly [23]. The temperature-dependent anisotropic elastic constants of the phases  $\gamma$  and  $\gamma'$  were taken from References [24] and [25], respectively.

The interfacial dislocation networks in the turbine blades, which are the physical origins of the deformation-induced internal stresses [8], were not analyzed experimentally. Rather, they were determined indirectly from the values obtained by the analysis of spacings of the dislocations in the interfacial dislocation networks of samples of the alloy SRR 99 which had been tensile creep deformed at 1050 °C at different stresses [14]. The dislocation networks at (001) interfaces reduce the coherency stresses and build up the deformation-induced internal stresses which are of opposite sign compared to the coherency stresses (see Figure 1(b)). Therefore, the measured dislocation spacings of these interfaces had to be corrected for the spacings of dislocation networks which just relieve the coherency stresses. The temperature dependence of the used input value of the lattice misfit was not determined directly from the analysis of dislocation networks, but from the well-determined correlation of the change of the lattice parameters after tensile creep deformation obtained by X-ray diffraction on samples deformed at different temperatures [2, 3, 5, 8, 9]. The local stress data were taken from the analytically calculated values, see Figure 3.

The local temperatures were used as fit parameters for the calculations and were adjusted by systematical variations in order to obtain a good correlation of the calculated lattice parameters in three dimensions with the X-ray line profiles. From this, the local temperatures in the turbine blades can be inferred. A second possibility to determine the local temperatures is the comparison of the measured lattice misfit values with the dependence of the lattice misfit on local temperatures and stresses determined by a systematical variation of the input of the FEM calculations.

**Procedure of the FEM calculations.** In the FEM model, the internal stresses are considered by a modification of the actual thermal expansion coefficients of the two phases  $\gamma$  and  $\gamma'$  in a similar way as in the case of creep-deformed samples by Feng et al. [18]. This modification serves to introduce the resultant strains caused by the extra half-planes of the deformation-induced interfacial dislocations. These dislocations are of different character at the interfaces parallel and perpendicular to the stress axis (see Figure 1 and the experimental results of Keller et al. [14]) and serve to introduce the coherency stresses prevailing after deformation (only at the (100)/(010) interfaces, because the coherency stresses are relaxed at the (001) interfaces).

In order to obtain the complete stress state for room temperature, a cooling procedure from the service temperature to room temperature was used in the FEM calculations with the modified expansion

coefficients. From the strain distributions at room temperature, the lattice-parameter distributions and the average lattice-mismatch values are determined in the  $\langle 100 \rangle$  directions.

## Results

### Initial state

The microstructure of an original turbine blade prior to service was characterized by SEM and TEM. The cuboidal  $\gamma'$  precipitates are clearly visible in the SEM micrograph of Figure 4(a) and in the dark field TEM micrograph of Figure 4(b). An X-ray line profile of the "virgin" turbine blade will be discussed later together with line profiles of the turbine blade subjected to service-like conditions (Figure 6).

### Turbine blade subjected to service-like conditions

**Microstructure.** In Figure 5, a schematical drawing of the turbine blade is shown with some micrographs of local  $\gamma/\gamma'$  microstructures. Near the cooling channels, the originally cuboidal shape of the  $\gamma'$  particles is preserved. The size, however, is larger than in the initial state, and the precipitates exhibit a rounded shape. Near the leading and the trailing edges, directional coarsening can be observed. The  $\gamma$  phase surrounds at all investigated positions the  $\gamma'$  phase.

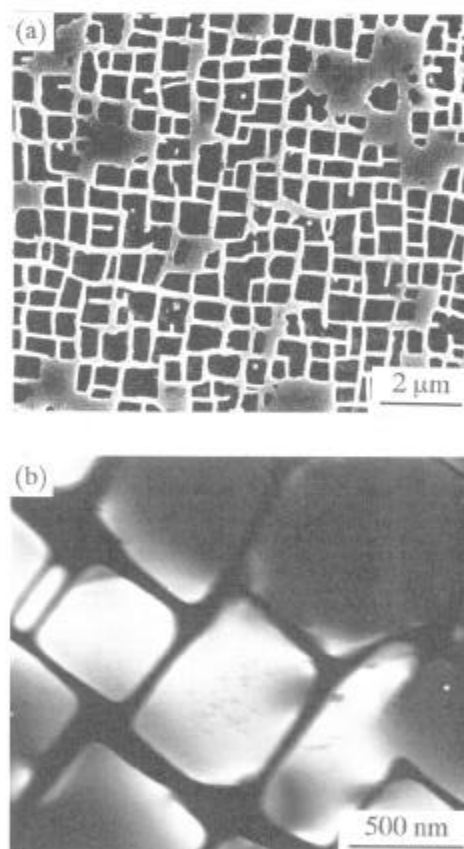


Figure 4:  $\gamma/\gamma'$  microstructure of the original turbine blade (before service). (a) SEM,  $\gamma'$ : dark; (b) TEM dark field,  $\gamma'$ : bright.

The mean edge lengths of the two phases in the  $\langle 100 \rangle$  directions were determined with a digitizing table and used as a basis for the dimensions of the FEM mesh. In the case of the modelling near the trailing edge (site 4 in Figure 5), the mean size of the  $\gamma'$  phase was determined as 1370 nm in the direction  $[100]$  (and in the equivalent direction  $[010]$ ) and 570 nm in the direction  $[001]$ . The FEM mesh, which models only one eighth of the  $\gamma'$  particle together with the corresponding half of the surrounding  $\gamma$  phase, has a rectangular shape with the dimensions  $773 \times 773 \times 373 \text{ nm}^3$  (i.e. the whole  $\gamma$  channel width for site 4 is assumed to be 176 nm).

The investigations on section III show microstructural changes which are qualitatively similar to those obtained on section II. The degree of coarsening, however, is less pronounced. The situation is more complicated at section I, since the middle of the section in the region near the cooling channels is directly above the platform, while the leading and trailing edges have a distance of some mm from the platform. This situation arises from the curved shape of the platform, see Figure 2. Therefore, the observation of a  $\gamma/\gamma'$  raft structure near the edges of the blade in section I is plausible. The region near the cooling channels exhibits  $\gamma'$  particles which are coarsened compared to the  $\gamma'$  precipitates of the "virgin" blade.

X-ray line profiles.  $(002)$  and  $(200)/(020)$  X-ray line profiles measured on cross section II and on different longitudinal sections are presented in Figure 6. The locations, where the individual measurements were made, correlate with the sites corresponding to the micrographs given in Figure 5. The intensities of the profiles are normalized to their maximum and plotted versus the glancing angle  $\theta$ .

In addition, a typical line profile of a turbine blade in the initial state is given.

The profile of the initial state is symmetrical, indicating a vanishing lattice mismatch ( $\delta = 0$ ). The profiles of the loaded and the unloaded blade are different in two ways: i) The profiles of the blade subjected to service are broadened compared to the profile of the blade prior to service and ii) the profiles of the blade subjected to service are asymmetrical. The reasons are, first of all, crystal distortions (e.g. dislocations) which lead to line broadening, and, in addition, long-range internal stresses which lead to the shift of the subprofiles of the two phases. The  $(002)$  profiles show in all cases a shoulder on the right side of the maximum. The shoulder can be attributed to the  $\gamma$  phase and the maximum to the  $\gamma'$  phase. The shape of the profiles is equivalent to the case of tensile creep-deformed samples [2, 3, 8, 9]. The shoulder (or second peak), however, is more pronounced the larger the distance from the cooling channels is. The values of the lattice misfit which are evaluated from the separation of the two subprofiles are positive for all  $(002)$  profiles (see Table I). This situation is similar to the investigations on other turbine blades reported earlier [5-7].

The shapes of the  $(200)$  and  $(020)$  profiles are more complex. The  $(020)$  profile of site 1 has two maxima, with the higher maximum at the right side. The type of asymmetry is again the same as for tensile creep-deformed samples. The same holds for the  $(200)$  profile of site 2, where the second ( $\gamma$ ) profile only builds up a shoulder on the left side. The profile of site 3, however, is symmetrical, and the profile of site 4 shows an inverse asymmetry compared to creep-de-

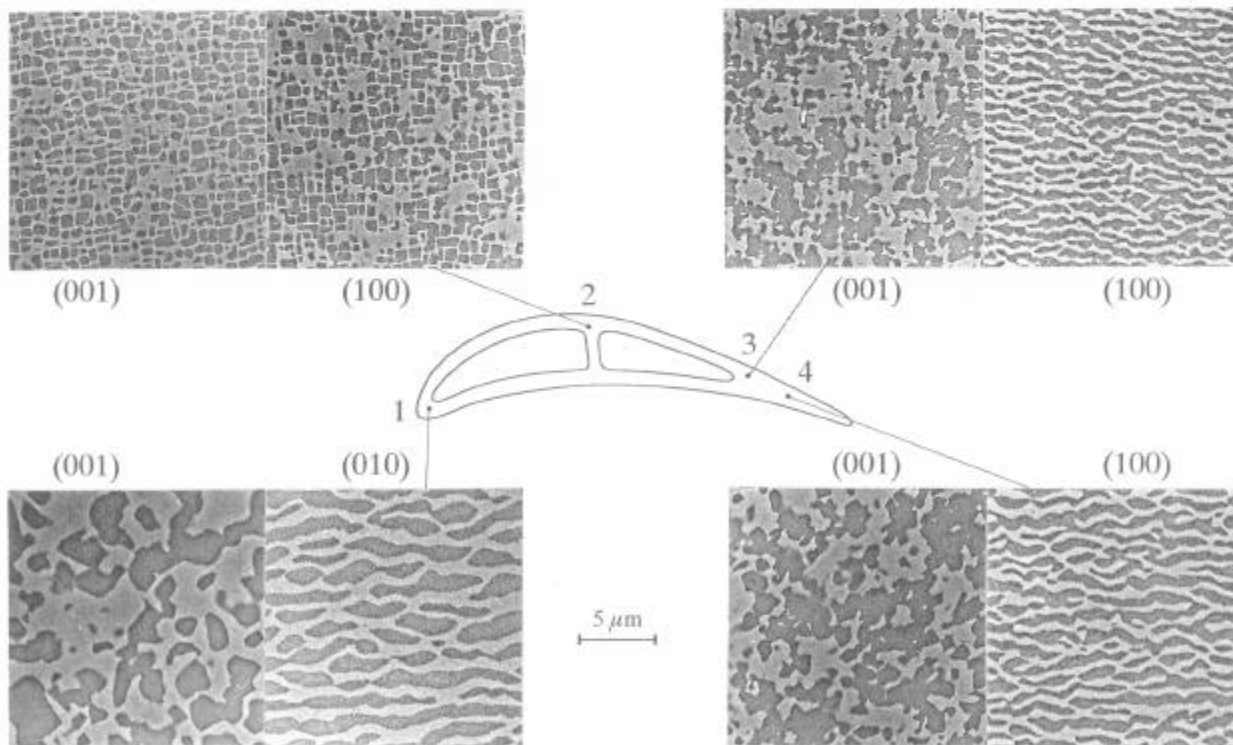


Figure 5: Microstructure of a turbine blade subjected to increased temperature tests for several hundred hours, nickel-base superalloy CMSX-6. The SEM micrographs show the  $\gamma/\gamma'$  microstructure at the positions indicated in the schematical drawing, section II. The  $(100)/(010)$  micrographs belong to adjacent longitudinal sections.  $\gamma'$ : dark. The stress axis is vertical in the case of the longitudinal sections  $(100)$  and  $(010)$ .

Table I: Lattice misfit obtained by the analysis of the X-ray line profiles of Figure 6. The lattice misfit of the undeformed state of the alloy CMSX-6 is  $\delta \approx 0$ .

site no.	$\delta_{[100]/[010]}$	$\delta_{[001]}$
1	$-1.7 \times 10^{-3}$	$+2.6 \times 10^{-3}$
2	$-1.5 \times 10^{-3}$	$+1.8 \times 10^{-3}$
3	$-1.5 \times 10^{-3}$	$+2.5 \times 10^{-3}$
4	$-1.7 \times 10^{-3}$	$+2.8 \times 10^{-3}$

formed samples. At present, the shapes of these profiles can only be understood by considering also the (300) super-lattice reflection of the  $\gamma'$  phase. This super-lattice reflection is asymmetrical, with a considerably more slowly decreasing tail on the (left) lower angle side. Therefore, the measured (200) profiles consist of the asymmetrical  $\gamma'$  peak (on the right) and, on the left, of the  $\gamma$  peak. The superposition of the asymmetrical  $\gamma'$  peak and the  $\gamma$  peak can give rise to the shape of the (200) profiles of sites 3 and 4. The values of the lattice misfit are also given in Table I. The results obtained on the sections I and III are qualitatively equivalent to those of section II. The magnitude of the changes of the lattice misfit, however, is smaller at sections I and III.

Complementary investigations of the X-ray line profiles on other turbine blades [5-7] yielded similar results as those reported in the present work. One blade, however, was used under so-called emergency conditions. A (002) X-ray line profile measured near the leading edge of that blade showed a reversed asymmetry which is not understood in detail. The microstructure of that part of the

blade had a bimodal size distribution of the  $\gamma'$  particles, thus indicating that the temperature during service exceeded normal operation conditions. In the case of the (200) and (020) line profiles, the investigations reported in [5-7] showed an almost symmetrical shape. This is in contrast to the results of the present work. One possible reason is that the blade investigated in the present work was in service for 400 hours, whereas the blades of Refs. [5-7] for only about 70 hours.

**Transmission electron microscopy.** Figure 7(a) shows a TEM micrograph of a (100) oriented sample at site 4 near section II with dislocation networks at the  $\gamma/\gamma'$  interfaces (i.e. at the interfaces which are more or less parallel to the (100) lattice planes). Due to the strong curvature of the (100) and (010)  $\gamma/\gamma'$  interfaces, the interfacial dislocation networks cannot be analyzed in order to obtain the dislocation spacings in the principal (100) directions which would be necessary as input for the FEM calculations, if the real microstructure of the blade should be used. Complementary investigations on TEM samples with (001) orientation yielded also dense interfacial dislocation networks, see Figure 7(b).

**Convergent beam electron diffraction (CBED).** The CBED patterns of the [100] zone axis observed in the phases  $\gamma$  and  $\gamma'$  of a TEM slice prepared near site 4 (see Figure 7) are shown in Figures 8(a) and (b), respectively. The HOLZ lines clearly indicate that the four-fold symmetry of the undistorted crystal lattice is disturbed, and only a twofold symmetry remains. A systematic variation of the input lattice parameters for a kinematical simulation of the HOLZ lines of the two phases was performed. Fitting the patterns with calculated HOLZ lines indicates that the crystal lattice of the  $\gamma$  phase is strained in tension in the directions [100] and [010] and in com-

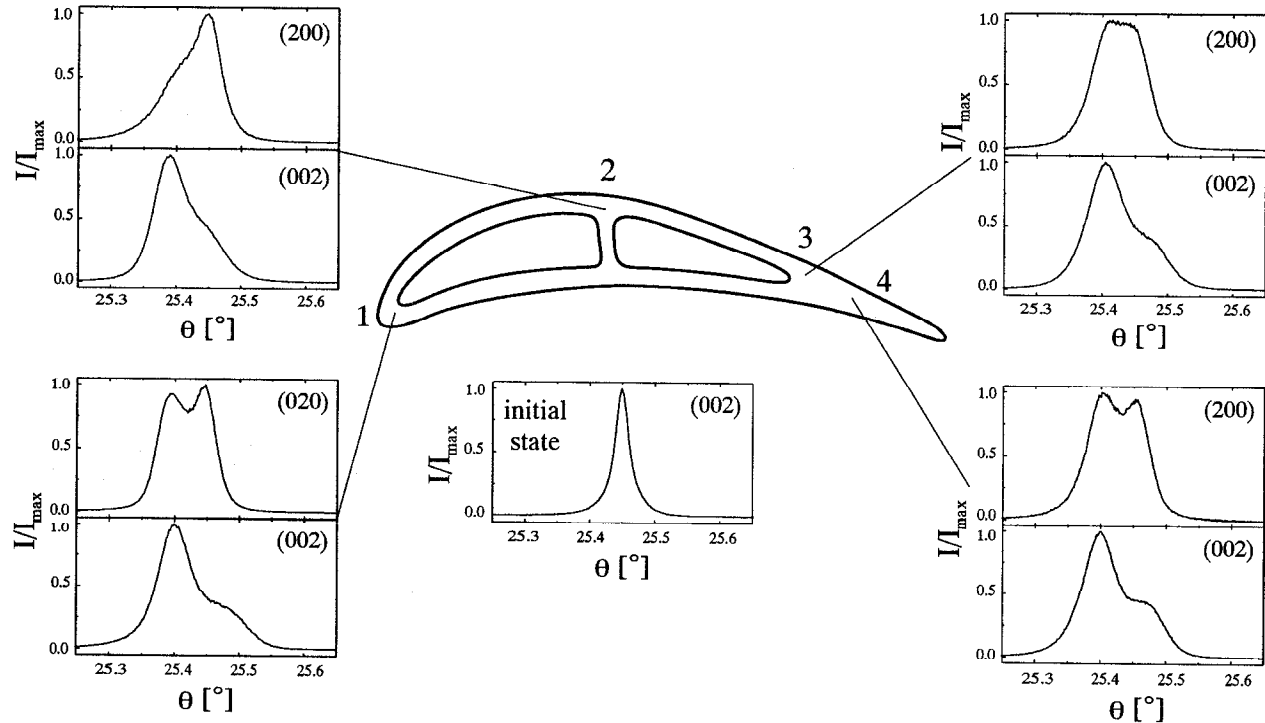


Figure 6: (002) and (200)/(020) X-ray line profiles of the turbine blade subjected to increased temperature tests, measured at the sites given in Figure 5. The line profile of the undeformed state of the alloy CMSX-6 is plotted in addition.  $\theta$ : glancing angle.

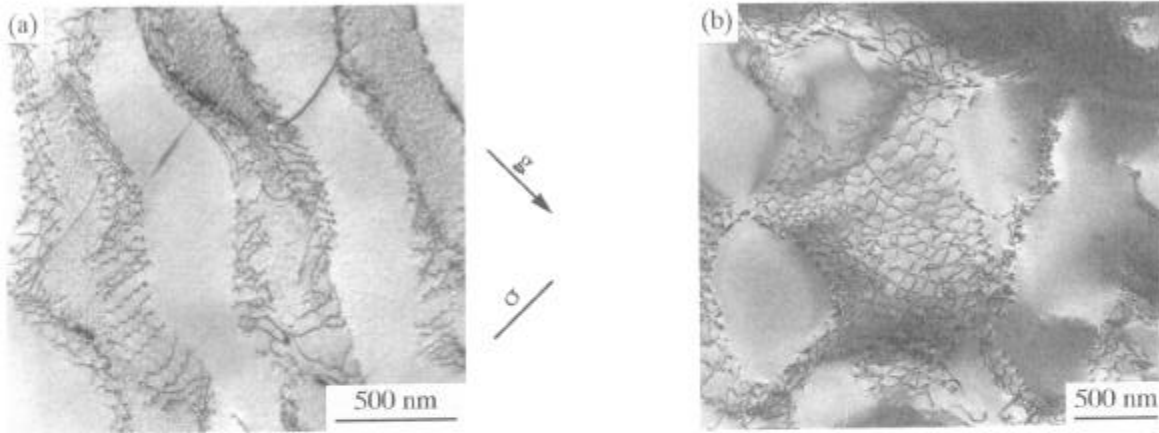


Figure 7: TEM micrographs of the  $\gamma/\gamma'$  structure with interfacial dislocation networks, turbine blade subjected to service-like conditions, site 4. (a) (100) section,  $g = (020)$  and (b) (001) section,  $g = (020)$ .

pression in the [001]-direction. In the  $\gamma'$  phase, the inverse is true: The lattice parameter in the [001] direction is strained in tension, the lattice parameters in the two perpendicular directions are strained in compression. Hence, the investigations prove the tetragonal lattice distortion of the two phases.

**FEM Calculations.** Systematical variations of the volume fraction of the  $\gamma'$  phase and of the dimensions of the  $\gamma/\gamma'$  plate structure proved that these two input parameters have only a minor effect on the lattice-parameter distributions and lattice-mismatch values at room temperature. The volume fraction of the  $\gamma'$  phase used for the modelling was 55 Vol.%, based on a quantitative evaluation of the SEM micrographs. The strains in the two phases are essentially determined by the temperatures, from which the samples are cooled to room temperature in the calculations, and the local stresses, which determined the dislocation networks at the interfaces. This

finding is not surprising, since the starting temperatures determine the amount of thermal stresses at room temperature, and the local stresses determine the deformation-induced internal stresses.

In Figure 9, calculated lattice parameters (solid lines in Figure 9) of the phases  $\gamma$  and  $\gamma'$  in the directions [001] (Figure 9(a)) and [100] (Figure 9(b)) are compared with the (002) and (200) X-ray line profiles (dashed lines), respectively, measured near the trailing edge of the turbine blade at site 4. Our computations do not take into account line broadening due to dislocations, etc.. A good correlation of the positions of the peaks of the calculated lattice parameter distributions with the measured profiles was obtained under the assumption of a local stress state equivalent to that after creep deformation at a temperature of 1050 °C under a stress of 100 MPa. The determined local temperatures (for the given stress values, see Figure 3) at sites 1, 3 and 4 are given in Table II. In the table, the local

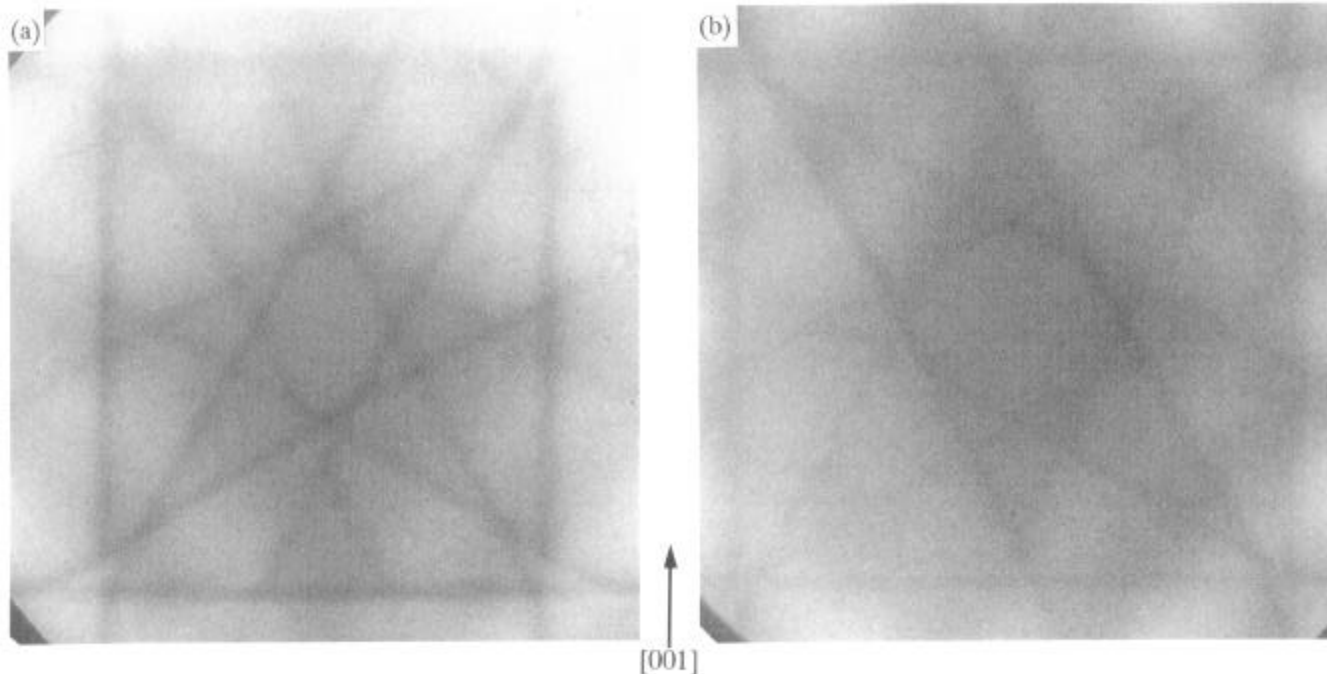


Figure 8: HOLZ line patterns of the [100] zone axis (longitudinal section of site 4). (a)  $\gamma$  phase, (b)  $\gamma'$  phase.

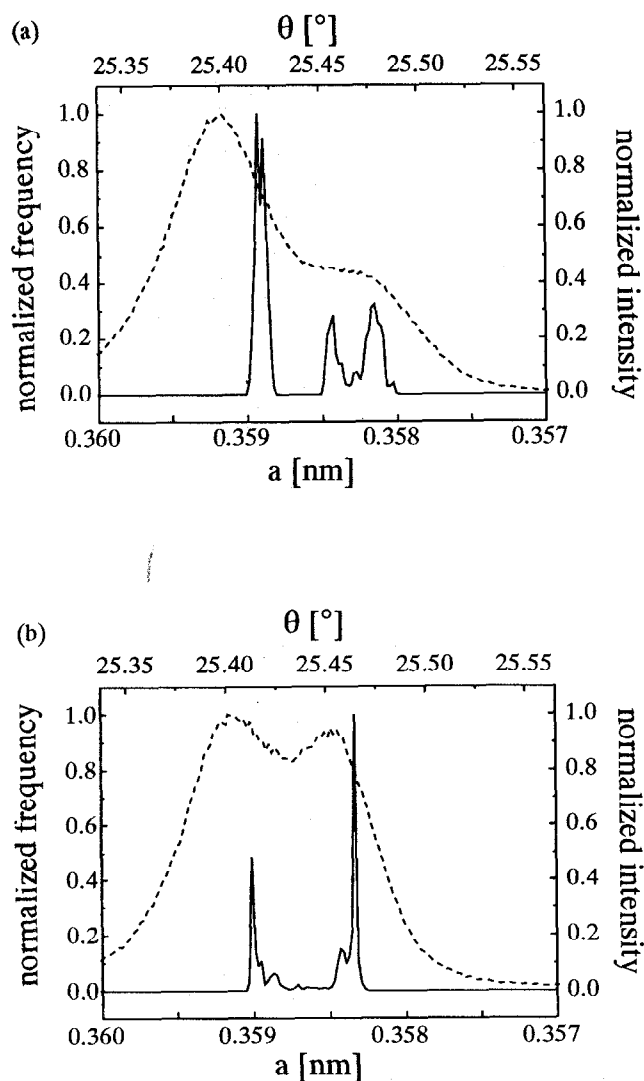


Figure 9: Comparison of calculated lattice parameters (solid lines) in the directions [001] (a) and [100] (b) with (002) and (200) X-ray line profiles (dashed lines) from a region near the trailing edge of a CMSX-6 turbine blade, which has been exposed to service; site 4, as indicated in Figure 5.  $\theta$ : glancing angle.

temperatures determined from the systematical variation of the temperature to obtain a good correlation of the shape of the lattice parameter distributions with the line profiles are called “fit of the shape”.

The temperatures determined by the use of the measured misfit values and their comparison with the dependencies calculated from systematical variations of the FEM input parameters are also given in Table II and called “comparison of  $\delta$ ”. In the case of the use of  $\delta$ , the temperatures are up to 100 °C higher than the values determined from the comparison of the shape of the lattice parameter distributions. At site 2, where the  $\gamma'$  particles have cuboidal shape, no valid temperature could be estimated by the FEM calculations. The reason is that the present input parameters are based on the dislocation spacings of dislocation networks of the  $\gamma/\gamma'$  raft structure.

Table II: Comparison of temperatures obtained by the fit of the shape of the lattice parameter distribution and from the comparison of  $\delta$ .

site no.	$\sigma$	T (fit of the shape)	T (comparison of $\delta$ )
1	90 MPa	1050 °C	1169 °C
2	40 MPa	—	—
3	230 MPa	940 °C	977 °C
4	100 MPa	1050 °C	1146 °C

## Discussion

### $\gamma/\gamma'$ morphology

The changes of the  $\gamma/\gamma'$  morphology are understandable with regard to the loads acting in the blade during service. The region near the cooling channels shows coarsened  $\gamma'$  precipitates with cuboidal shape. In these regions, the combination of the relatively low material temperatures and the local stresses did not lead to rafting. In the regions with higher material temperatures near the leading and trailing edges, however, the material temperature was higher and, in combination with the external centrifugal stress, rafting occurred. This observation of rafting in a turbine blade after engine operation is in agreement with the results of Draper et al. [4]. These authors reported, for example, that rafting occurred in up to 60 % of the span length in blades of the nickel-base superalloy NASAIR 100. The degree of rafting depended on the test conditions, i.e. the operation time, the temperatures and the externally applied (centrifugal) stresses. Earlier investigations of other turbine blades in the authors' group [5-7] showed similar  $\gamma/\gamma'$  morphologies in turbine blades already after about 70 hours of service.

In the turbine blade investigated in the present work, the  $\gamma$  phase remains the surrounding matrix phase with included  $\gamma'$  plates. The investigations of  $\gamma/\gamma'$  morphologies of creep-deformed samples of the alloys SRR 99 and CMSX-4, however, showed that the connectivity had changed after about 1 % plastic strain. The reason may lie in the details of the thermal and mechanical exposure and, perhaps more important, in the fact that the volume fraction of the  $\gamma'$  phase is smaller in the alloy CMSX-6 compared to the two other alloys (SRR 99 and CMSX-4). A final explanation of the reason for these different behaviours cannot be given yet.

### Lattice distortions

The lattice distortions were measured with two complementary techniques, i.e. high-resolution X-ray diffraction and CBED. These methods have different lateral resolutions. The X-ray method integrates the lattice parameter distributions over a volume of 0.5 mm  $\times$  0.5 mm  $\times$  5 - 10  $\mu$ m and hence provides a mean value of the lattice parameter changes with high accuracy. In the way applied here, the CBED technique yields no absolute but only relative lattice parameter values, but has an excellent lateral resolution with a cross section of the electron beam of about 20 nm. Therefore, the two methods provide complementary information. It is satisfying to note, that both methods yield qualitatively the same tetragonal lattice distortions, namely tensile and compressive distortions in the  $\gamma'$  and the  $\gamma$  phase in the direction [001], respectively. Therefore, both methods give experimental evidence of lattice distortions compatible with those shown schematically in Figure 1.

For the CBED investigations performed so far (see e.g. Figure 8), the [100] zone axis was used. Since low indexed zone axes (as the  $\langle 100 \rangle$  type zone axes) are highly distorted by dynamical scattering effects, only limited quantitative information can be obtained from the kinematical simulation of the HOLZ line patterns of such zone axes. In the present case, the change of the line pattern from a four-fold symmetry in the initially undeformed state to a pattern with two-fold symmetry in the blade exposed to service confirms the tetragonal lattice distortion of both phases  $\gamma$  and  $\gamma'$ . The HOLZ line patterns (Figure 8) are qualitatively the same as the patterns observed by Keller et al. [15], who investigated a sample of the nickel-base superalloy SRR99 creep-deformed in tension at a temperature of 1050 °C at a stress of 305 MPa. In the present case, the degree of the tetragonal distortion is somewhat smaller than that observed in the sample of Keller et al.. This indicates that the lattice distortions are smaller in the present case. A comparison of preliminary kinematical HOLZ line simulations of the patterns of Figure 8 with dynamical simulations showed a difference of the positions of the calculated HOLZ lines. Future work will be performed which will simulate the  $\langle 100 \rangle$  zone axes with dynamical computer simulations of the HOLZ lines in combination with experimental investigations on the  $\langle 114 \rangle$  zone axes.

#### Estimation of the local loads

The comparison of X-ray investigations with the results of FEM calculations allows the estimation of either the stresses or the temperatures present locally during service, if the other of the two parameters is known. In the present case, values of the stresses are given which had been calculated analytically (see Figure 3). These values should be more reliable than the computed temperatures, since during service of the turbine blade, several factors can lead to temperature fluctuations. Therefore, in our studies, the determination of the local temperatures seem to be more appropriate.

The local temperatures determined in the present work by the fit of the shape of the lattice parameter distribution are in good correlation with the specific test conditions of the engine. This fit yields lower temperatures than the use of the averaged misfit values (see Table II). The temperatures determined by the latter method at sites 1 and 4 are too high. This shows that the comparison of more global values such as the misfit gives unsatisfactory results, especially in the case, where the X-ray line profiles have shapes which cannot be explained in a straightforward manner. In the case of creep-deformed samples [18], the values of the lattice misfit could be used for the comparison of measured profiles with the calculated lattice parameter distributions, since the shape of the profiles agreed fairly well with the calculated results. This may be explained by the different morphologies of the two cases: In the turbine blade, the  $\gamma$  phase surrounds  $\gamma'$ , in the creep samples, the  $\gamma'$  phase surrounds  $\gamma$ .

Figure 9 shows some differences between the measured X-ray profiles and the calculated lattice parameter distributions: i) The measured profiles are much more broadened than the calculated distributions, because different line broadening contributions, i.e. dislocations in the two phases and at the interfaces, residual coherency strains, the particle size effect of the small coherently scattering particles and the difference between the idealized model and the real microstructure (Figure 5) were not taken into account. ii) The intensity relation between the left ( $\gamma$ ) and the right ( $\gamma'$ ) peak of the lattice parameter distribution in the [100] direction corresponds not

to the (200) line profile (Figure 9(b)). The reason for this discrepancy may be connected with the asymmetry of the (300) line profile mentioned above. The shape of this profile, however, is not understood yet. Therefore, only the separation of the peaks of the calculated distribution can be compared with the splitting-up of the measured profile into two peaks. iii) The FEM calculations of this work consider the dislocation structure which was investigated in samples after pure tensile creep deformation. The blade, however, is subjected to the superposition of complex loads such as centrifugal stresses, bending or thermomechanical fatigue. These factors cause complex triaxial stress states which were not taken into consideration.

The calculations are based on an assumption which was not discussed until now. The dislocation network data used for the modelling were obtained on samples creep deformed until fracture. The dislocation structure in the turbine blade, where the total allowed strain is 1 or 2 % and the maximal experienced local strain is in the order of up to 4 or 5 %, may be different compared to samples deformed to fracture with strains of about 20 %. Since earlier investigations showed that the change of the line profiles of creep-deformed samples is completed after strains of about 1 % [5], the local strains experienced by the blade seem to be sufficient for the full build up of the internal stress state. Another problem arises from the possible differences between the dislocation structure in the blade and in a creep sample which would experience equal stresses. The quite good agreement between the measured line profiles and the calculated lattice parameters shows that the method is successful. In further work, the real dislocation structure of the turbine blade will be investigated in detail.

#### Conclusions

The main conclusions of the investigations on a turbine blade subjected to service-like conditions are:

1. In the regions exposed to high metal temperatures and (centrifugal) stresses, directional coarsening and rafting occur.
2. X-ray line profiles indicate elastic, tetragonal lattice distortions.
3. CBED investigations confirm the predicted tetragonal lattice distortions of the two phases  $\gamma$  and  $\gamma'$ .
4. From the comparison of calculated lattice parameters with experimentally measured X-ray line profiles, the locally acting temperatures are determined for given stress values. These temperatures were determined to be up to about 1050 °C near the leading and trailing edges.
5. It can be concluded from the microstructural characterization that the leading and trailing edges of the turbine blade are under stress states which are similar to those of samples creep-deformed in tension.
6. In summary, it has been demonstrated that a sufficiently detailed microstructural characterization of blades exposed to service conditions permits an estimate of the local stress states and temperatures experienced during service.

#### Acknowledgment

The authors thank Dr.-Ing. D. Goldschmidt (formerly MTU, Munich), now Siemens AG/KWU, Mülheim, and Mr. W. Buchmann, MTU, for support of this work, and the company MTU for providing the investigated turbine blades. The authors are grateful to Mr. S. Mechsner for performing some of the X-ray measurements.

### Literature

1. T. M. Pollock and A. S. Argon, "Creep Resistance of CMSX-3 Nickel Base Superalloy Single Crystals", Acta metall. mater., 40 (1992), 1-30.
2. H. Biermann, M. Strehler and H. Mughrabi, "High-Temperature X-Ray Measurements of the Lattice Mismatch of Creep-Deformed Monocrystals of the Nickel-Base Superalloy SRR 99", Scripta metall. mater., 32 (1995), 1405-1410.
3. H. Biermann, M. Strehler and H. Mughrabi, "High-Temperature Measurements of Lattice Parameters and Internal Stresses of a Creep-Deformed Monocrystalline Nickel-Base Superalloy", Met. Trans. A, 27A (1996), 1003-1014.
4. S. Draper, D. Hull and R. Dreshfield, "Observations of Directional Gamma Prime Coarsening during Engine Operation", Metall. Trans. A, 20A (1989), 683-688.
5. S. Spangel, "Röntgenographische Untersuchung lokaler Gitterparameter in Labor- und Turbinenschaufelproben aus einkristallinen Nickelbasis-Superlegierungen", (diploma thesis, Universität Erlangen-Nürnberg, Germany, 1994).
6. H. Biermann, S. Spangel and H. Mughrabi, "Investigation of Local Lattice Parameter Changes in Monocrystalline Nickel-Based Turbine Blades after Service", in: Proc. EUROMAT 95, Padua/Venice, Italy, Vol. 2, (ed. Associazione Italiana di Metallurgia), Milano, Italy (1995), 255-260.
7. H. Biermann, S. Spangel and H. Mughrabi, "Local Lattice Parameter Changes in Monocrystalline Turbine Blades Subjected to Service-Like Conditions", Z. Metallkde., 87 (1996), 403-410.
8. H.-A. Kuhn, H. Biermann, T. Ungár and H. Mughrabi, "An X-Ray Study of Creep-Deformation Induced Changes of the Lattice Mismatch in the  $\gamma'$ -Hardened Monocrystalline Nickel-Base Superalloy SRR 99", Acta metall. mater., 39 (1991), 2783-2794.
9. H. Mughrabi, H. Biermann and T. Ungár, "X-Ray Analysis of Creep-Induced Local Lattice Parameter Changes in a Monocrystalline Nickel-Base Superalloy", in "Superalloys 1992", Proc. 7th Int. Symp. on Superalloys (eds. S. D. Antolovich, R. W. Stusrud, R. A. MacKay, D. L. Anton, T. Khan, R. D. Kissinger and D. L. Klarstrom), TMS, Warrendale, Pennsylvania (1992), 599-608.
10. U. Glatzel and A. Müller, "Neutron Scattering Experiments with a Nickel Base Superalloy, Part I: Material and Experiment", Scripta metall. mater., 31 (1994), 285-290 and U. Glatzel, "Neutron Scattering Experiments with a Nickel Base Superalloy, Part II: Analysis of Intensity Profiles", Scripta metall. mater., 31 (1994), 291-296.
11. U. Glatzel and A. Müller, "Calculated and Measured Internal Stresses of Creep-Deformed Single Crystal Nickel-Based Superalloys", in: "Numerical Predictions of Deformation Processes and the Behaviour of Real Materials", Proc. 15th Risø Int. Symp. on Materials Science, (eds. S. I. Andersen, J. B. Bilde-Sørensen, T. Lorentzen, O. B. Pedersen and N. J. Sørensen), Risø National Laboratory, Roskilde, Denmark (1994), 319-324.
12. T. Gnäupel-Herold and W. Reimers, "Stress States in the Creep Deformed Single Crystal Nickelbase Superalloy SC16", Scripta metall. mater., 33 (1995), 615-621.
13. A. Royer, P. Bastie, D. Bellet and J. L. Strudel, "Temperature Dependence of the Lattice Mismatch of the AM1 Superalloy. Influence of the  $\gamma'$  Precipitates' Morphology", Phil. Mag. A, 72 (1995), 669-690.
14. R. R. Keller, H. J. Maier and H. Mughrabi, "Characterization of Interfacial Dislocation Networks in the Creep-Deformed Nickel-Base Superalloy SRR 99", Scripta metall. mater., 28 (1993), 23-28.
15. R. R. Keller, H. J. Maier, H. Renner and H. Mughrabi, "Local Lattice Parameter Measurements in a Creep-Deformed Nickel-Base Superalloy by Convergent Beam Electron Diffraction", Scripta metall. mater., 27 (1992), 1167-1172, and Scripta metall. mater., 28 (1993), 661.
16. J. Li and R. P. Wahi, "Investigation of  $\gamma/\gamma'$  Lattice Mismatch in the Polycrystalline Nickel-Base Superalloy IN 738LC: Influence of Heat Treatment and Creep Deformation", Acta metall. mater., 43 (1995), 507-517.
17. L. Müller, U. Glatzel and M. Feller-Kniepmeier, "Calculation of the Internal Stresses and Strains in the Microstructure of a Single Crystal Nickel-Base Superalloy During Creep", Acta metall. mater., 41 (1994), 3401-3411.
18. H. Feng, H. Biermann and H. Mughrabi, "3D Finite Element Modelling of Lattice Misfit and Long-Range Internal Stresses in Creep-Deformed Nickel-Base Superalloy Single Crystals", Mater. Sci. Eng., in press.
19. H. Brooks, "Metal Interfaces", American Society of Metals (1952), 20-64.
20. M. V. Nathal, J. O. Diaz and R. V. Miner, "High Temperature Creep Behaviour of Single Crystal Gamma Prime and Gamma Alloys", in Proc. MRS Symp., Vol. 133, (eds. C. T. Liu, A. I. Taub, N. S. Stoloff, C. C. Koch), MRS, Pittsburgh, Pennsylvania (1989), 269-274.
21. C. Carry, S. Dermarkar, J. L. Strudel and B. C. Wonsiewicz, "Internal Stresses due to Dislocation Walls Around Second Phase Particles", Metall. Trans. A, 10A (1979), 855-860.
22. P. A. Stadelmann, "EMS — A Software Package for Electron Diffraction Analysis and HREM Image Simulation in Materials Science", Ultramicroscopy, 21 (1987), 131-146.
23. W. Hermann, "Elastizität und Anelastizität technisch wichtiger Hochtemperaturlegierungen", (doctorate thesis, Universität Erlangen-Nürnberg, Germany, 1995).
24. H.-A. Kuhn, "Anwendung von Grenzwertkonzepten und Phasenmischungsregeln auf die elastischen Eigenschaften von Superlegierungen zwischen Raumtemperatur und 1200 °C", (doctorate thesis, Universität Erlangen-Nürnberg, Germany, 1987).
25. R. W. Dickson, J. B. Wachtmann and S. M. Copley, "Elastic Constants of Single-Crystals Ni<sub>3</sub>Al from 10 °C to 850 °C", J. Appl. Phys., 40 (1969), 2276-2279.